

Investigation on the Impact of CMEs and CIRs on the Martian Ionospheric Species

L. Ram¹, D. Rout², R. Rathi¹, S. Mondal^{1,†}, S. Sarkhel^{1*}, and J. Halekas³

^{*}Sumanta Sarkhel, Department of Physics, Indian Institute of Technology Roorkee, Roorkee - 247667, Uttarakhand, India (sarkhel@ph.iitr.ac.in)

¹Department of Physics,
Indian Institute of Technology Roorkee,
Roorkee - 247667
Uttarakhand, India

²GFZ German Research Centre for Geosciences,
Potsdam, Germany

³Department of Physics and Astronomy
414 Van Allen Hall
University of Iowa
Iowa City, IA – 52242
USA

[†]Now at: Physical Research Laboratory,
Ahmedabad-380009,
Gujarat, India

Abstract

The measurements from the Mars Atmosphere and Volatile EvolutioN (MAVEN) spacecraft, orbiting Mars are used for investigating the impact of coronal mass ejection (CMEs) and corotating interaction region (CIRs) on the ionospheric species variations in the Martian ionosphere. We have chosen 15 CME and 15 CIR events from the existing catalogs in order to compare their impact on the Martian ionospheric species. We have observed depletions in the electron density, ion density and enhancement in electron temperature during the specific case of CME (03-05 October 2018) and CIR (29 May-04 June 2016). Our analyses show that the depletion in the outbound phase was more pronounced compared to the inbound phase during both events. However, during specific CIR, depletion in the plasma density occurred for a greater number of orbit profiles compared to specific CME. We have provided a comparative average scenario of variation of ionospheric constituents with respect to altitude (150-500 km) during 15 CME and 15 CIR events. The analyses suggest that the electron and ion mean density were more depleted during the CIRs compared to the CMEs. The depletions were more prominent in the outbound phase compared to the inbound phase. The lighter ions peak mean altitude and density were observed at lower altitude during the CIRs compared to the CMEs. Thus, this study suggests that the impact on the Martian ionospheric species during CIRs is more prominent compared to CMEs.

Keywords: Mars Atmosphere and Volatile EvolutioN (MAVEN), Coronal Mass Ejection (CME), Corotating Interaction Region (CIR), Martian Ionospheric Species.

1. Introduction

Solar energetic events, namely Coronal Mass Ejections (CMEs) and Corotating Interaction Regions (CIRs), are the principal drivers of the major space weather phenomena in the planetary atmosphere. CMEs are defined as a huge burst of plasma and magnetic field originating from the outer surface of the sun (Gosling 1990; Gopalswamy 2006; Jian et al. 2006). CMEs traverse all the way from the solar corona to interplanetary space, preceded by a forward shock (Tousey 1973; Chen 2011). They are commonly characterized by a strong rotating magnetic field, low β (ratio of plasma pressure and magnetic pressure), low ion temperature, high proton density, and enhancement in velocity (Gosling et al. 1991; Neugebauer & Goldstein 1997; Gosling & Forsyth 2001; Cane & Richardson 2003; Russell & Shinde 2005; Wimmer-Schweingruber et al. 2006; Zurbuchen & Richardson 2006).

During the declining phase of the solar cycle, the high-speed solar wind originates from the coronal holes (at higher solar latitudes) and the slow solar wind streams originate at lower solar latitudes (Gosling & Pizzo 1999; Belcher & Davis Jr. 1971; Smith & Wolfe 1976; Borovsky & Denton 2006; Richardson 2018). The high-speed solar wind interacts with the preceding slow solar wind streams to form an interaction region that co-rotates with the sun. These are known as Corotating Interaction Regions (CIRs) (Dubinin et al. 2009; Wei et al. 2012; Rout et al. 2017). The boundary that separates the high-speed streams from the slow streams is called the stream interface (SI). It is associated with an increase in the proton temperature and a high-pressure region (bounded by forward and reverse shocks) at large heliospheric distances (Burlaga 1974). CMEs and CIRs drive the major space weather events on the Earth and other planets (like Venus and Mars) of our solar system. On Earth, they initiate various geomagnetic events viz. storms and substorms. The Earth enjoys the advantage of a global magnetic shield, whereas Mars lacks such a global intrinsic magnetic shield, which consequently allows the solar wind to interact directly with the Martian atmosphere (Cloutier et al. 1969; Connerney et al. 2015). Martian bow shock develops as an obstacle in the form of a shock boundary, where the normal component of the supersonic solar wind decreases to subsonic speeds. Inside the shock boundary, there is a region of shocked and turbulent solar wind plasma termed the magnetosheath (Dubinin et al. 1997; Lundin et al. 1990). At the lower boundary of that region, the shocked solar wind plasma interacts with the upper atmosphere of Mars.

The photo-ionization of the Martian upper atmosphere by solar extreme ultraviolet (EUV) radiation forms the dayside ionosphere (McElroy et al. 1977; Fox & Dalgarno 1979). The current induced in the ionosphere by the motional electric field of the solar wind plays a

crucial role in the formation of the induced magnetosphere (Michel 1971). A tangential discontinuity that marks the transition from the hot plasma in the induced magnetosphere to the cold dense ionospheric plasma is termed as ionopause (Chu et al. 2021). The Martian ionopause altitude is affected by various space weather events (Schunk & Nagy 2009; Krishnaprasad et al. 2019; Thampi et al. 2021).

The Martian upper atmosphere responds significantly to the enhancement in the solar wind density, velocity, dynamic pressure, and variable IMF (interplanetary magnetic field). The solar wind interaction with the Martian upper atmosphere leads to the escape of various ions and neutral species. The escape of oxygen ions and precipitation of heavy ions in the Martian magnetosphere have been reported using data from ASPERA-3/Mars Express (MEX) (Hara et al. 2011; Wei et al. 2012). Using MAVEN observations, Thampi et al. (2018) showed that the ionopause is located at lower altitude during the passage of two consecutive ICMEs. Further, the work of Krishnaprasad et al. (2019) found a depletion in the nightside electron density for a longer period of time. The electron temperature was also enhanced during the period of electron density depletion. In addition, several other studies have also demonstrated the depletion and energization of the Martian ionosphere during CME and CIR events (Ma & Nagy 2007; Jakosky et al. 2015; Benna et al. 2015; Lee et al. 2017; Richardson 2018; Withers et al. 2018; Huang et al. 2019; Thampi et al. 2021). However, there is a lack of comprehensive understanding of how ionospheric species changes differently during CME and CIR events. Therefore, it is interesting to investigate the impacts of CMEs and CIRs on the Martian ionosphere. In this study, we report a comparative analysis of the Martian ionospheric species variation during 15 CME and 15 CIR events using MAVEN datasets.

2. Data

We have utilized the Space Weather Database of Notifications, Knowledge, and Information (DONKI) system and the catalogs of identified events (CMEs and CIRs) as provided by Huang et al. (2019); Geyer et al. (2021); Zhao et al. (2021) in our analyses. We have also utilized the Wang-Sheeley-Arge (WSA)-ENLIL+Cone model from the ENLIL Solar Wind Prediction to track the planetary positions, plasma blob, compressed streams, and IMF over the heliosphere (Odstrcil 2003; Mays et al. 2015).

After the selections of CME and CIR events, the different datasets are obtained from various instruments aboard the MAVEN spacecraft. These datasets can be accessed from the Planetary Data System and/or by using Python Data Analysis and Visualization tool

(PyDIVIDE). The instrument data files of Level-2, version_v17, revision number_r02, and revision_r04 are used in our analyses. The solar wind parameters (density, velocity, and dynamic pressure) data near Mars are obtained from the Solar Wind Ion Analyzer (SWIA) instrument aboard the MAVEN spacecraft. SWIA measures the solar wind ion flow around Mars in the upstream solar wind, magneto-sheath, and tail regions inside the bow shock. SWIA covers a broad energy range of 5 eV to 25 keV for solar ions (Halekas et al. 2015). In order to measure the IMF, we have obtained data using the Magnetometer (MAG) instrument. It has two independent triaxial fluxgate magnetometer sensors for magnetic field investigation and has an intrinsic sample rate of 32 vector samples/second (Connerney et al. 2015). The electron density and electron temperature data are obtained using the Langmuir Probe and Wave (LPW) instrument. LPW is optimized to measure electron density in the range of $\sim 10^2$ cm $^{-3}$ to 10 6 cm $^{-3}$ and temperature in a broad range of 500-50000 K (Andersson et al. 2015). The ions (O $^+$, O $_2^+$, CO $_2^+$, NO $^+$, C $^+$, N $^+$, & OH $^+$) density data is obtained using the Neutral Gas and Ion Mass Spectrometer (NGIMS). NGIMS is designed to measure the ions and neutrals in the range of 125-500 km altitude region of the Martian atmosphere using a dual ion source and a quadrupole analyzer (Mahaffy et al. 2015). It covers the mass range between 2-150 amu with unit mass resolution.

3. Results

3.1 Identification of passage of CME and CIR events at Mars:

The period from 03 to 05 October 2018 on Mars was characterized by a CME event and the period from 29 May to 04 June 2016 was characterized by a CIR event. Figure 1 shows the WSA-ENLIL+Cone simulation snapshots in the ecliptic plane during specific CME (03-05 October 2018) and CIR (29 May-04 June 2016) events. The color contour represents the radial solar wind velocity whereas the black-white dashed line represents the IMF in the inner heliosphere. The position of the planet Mars along with other inner planets is shown in the figure. Figures 1a-c show the three stages of development for the CME structure while entering, interacting, and leaving Mars. The CME event expands and becomes wider as it propagates through the heliosphere. During the event, a portion of the CME blob hit the planet Mars. Similarly, Figures 1d-f represent the three development stages during the CIR. The green and cyan color contours show the velocity of the solar wind and indicate the stream interaction region of the slow and fast solar wind near Mars. The ENLIL+Cone simulation predicts the event arrival and departure at Mars during the period.

During this period (CME [03-05 October 2018] and CIR [29 May-04 June 2016]), MAVEN observed that the solar wind parameters changed abruptly while crossing the Martian bow shock. In order to avoid contamination from the measurements near the bow shock and to select the undisturbed solar wind intervals in the upstream region, we utilized an algorithm proposed by Halekas et al. (2017). Figure 2 shows the variation of upstream solar wind (a) density, (b) velocity, (c) dynamic pressure, and (d) IMF ($|\mathbf{B}|$) during 01-06 October 2018 (for the CME event). The enhancement in the solar wind density started on 03 October 2018 and attained the peak value of $\sim 10 \text{ cm}^{-3}$. The solar wind velocity showed an enhancement starting from 03 October 2018, and the highest velocity $\sim 500 \text{ km/s}$ was observed on 04 October 2018. This event was also associated with enhancements in the dynamic pressure, and IMF ($|\mathbf{B}|$). The peak dynamic pressure and the peak value of IMF ($|\mathbf{B}|$) were 3 nPa and $\sim 15 \text{ nT}$ respectively at the beginning hour of 04 October 2018.

Similarly, Figure 3 shows the variation of upstream solar wind (a) density, (b) velocity, (c) dynamic pressure, and (d) IMF ($|\mathbf{B}|$) during 27 May- 03 June 2016 (for the CIR event). The solar wind velocity showed an enhancement starting from 29 May 2016 and attained the peak value of $\sim 450 \text{ km/s}$. The enhancement in the solar wind density started on 29 May 2016 and attained the peak value of $\sim 10 \text{ cm}^{-3}$. The peak dynamic pressure and the peak resultant IMF ($|\mathbf{B}|$) were $\sim 2.5 \text{ nPa}$ and $\sim 15 \text{ nT}$ respectively on 29 May 2016. Since the MAVEN spacecraft follows an elliptical orbit with an inclination angle of $\sim 75^\circ$, it observes the upstream solar wind measurements only intermittently, making it difficult to observe the exact event arrival time at Mars (Halekas et al. 2017). From Figures 2 & 3, it is evident that the solar wind interacted with the Martian ionosphere for a longer period during the CIR event in comparison to the CME.

3.2 Impact of the CME on the Martian ionosphere during 03-05 October 2018 event:

In order to study the impact of the incoming CME on the Martian ionosphere, we have analyzed the LPW and NGIMS data during CME (03-05 October 2018) event. Figures 4a-d show the LPW periapsis observations of electron density and temperature for inbound and outbound phases of the MAVEN orbits. Figures 4a-b show inbound whereas, Figures 4c-d depict outbound phases. The mean quiet time profile is shown with a black solid line and calculated by obtaining the mean of quiet orbits before the event (01- 02 October 2018) with a standard deviation. The event time orbits are depicted by different colors as shown in the figure. Here, we have selected only those disturbed orbits which are beyond the standard deviation. The inbound profiles showed that during CME, the electron density was significantly reduced in

orbits 7819 (04 October 2018) and 7825 (05 October 2018) at higher altitudes (above 350 km) associated with an enhancement in temperature up to \sim 10000 K. Similarly, the outbound profiles (orbits 7823, 7824, and 7826 on 05 October 2018) showed deviation beyond the standard deviation of mean quiet time profile. Here, in orbit 7826, a clear deviation from the mean quiet time profile and sharp density gradient can be observed. The electron density was depleted completely at around 400 km, which was similar to the ionopause-like situation. The other two profiles showed the deviation below 300 km but the electron density gradient was not as sharp compared to the orbit 7826. An enhancement of electron temperature was also observed, which approached more than 10000 K for the orbit 7826. The impact of CME event in the outbound orbits seemed more pronounced as compared to the inbound orbits, which implies that the impact of CME on the ionosphere during outbound was more in comparison to the inbound.

In addition to electron density and temperature, it is also important to explore the effects of CME on various ions. Figures 5a-n show the NGIMS observation for various ions (O^+ , O_2^+ , CO_2^+ , NO^+ , C^+ , N^+ , & OH^+) density in both inbound and outbound phases of the MAVEN orbits. Figures 5a-g (top panel) show inbound, while Figures 5h-n (bottom panel) depict the outbound phases. The inbound O^+ density profile (Figure 5a) shows a clear deviation from the mean quiet time profile for the orbit 7825. The other orbit profiles 7819, 7821, and 7823 also show deviation at higher altitudes (>300 km). The O^+ density shows a sharp gradient from 100 cm^{-3} to 0.01 cm^{-3} , starting from 300 km for orbit 7825, which is similar to the ionopause-like feature as defined by Vogt et al. (2015). Figure 5b shows the similar trend for O_2^+ ion density corresponding to the same orbits as observed for O^+ . The ion density profiles for other ions (CO_2^+ , NO^+ , C^+ , N^+ , & OH^+) depict a similar trend for the corresponding orbits as shown for O^+ and O_2^+ . Therefore, during the inbound phase, the electron and ion density show the ionopause-like feature for orbit 7825 in both LPW and NGIMS measurements. This indicates that there was at least one orbit profile in the inbound phase which depicts a sharp density gradient starting from \sim 300 km and had an ionopause formation around 450 km.

During the outbound phase (Figures 5c-g), there was a clear deviation from the mean quiet time profile for each ion and a sharp density gradient for O^+ , O_2^+ , CO_2^+ , & NO^+ ions can be observed for the orbit 7826. Here, the ionopause occurred comparatively at lower altitude (\sim 400 km) as compared to the inbound phase (\sim 450 km). For other ions (C^+ , N^+ , & OH^+), the corresponding orbit profiles also showed deviation from mean quiet time. However, due to less data availability, we could not confirm the ionopause. Although, the ionopause-like feature is

clearly visible for the rest of ions (O^+ , O_2^+ , CO_2^+ , & NO^+) during the orbit 7826 profile as mentioned earlier. Therefore, these observations indicate high variability for the outbound phase (nightside) of the Martian ionosphere during this CME event.

3.3 Impact of the CIR on the Martian ionosphere during 29 May-04 June 2016 event:

In order to study the impact of the incoming CIR on the Martian ionosphere, we have analyzed the LPW and NGIMS data during CIR (29 May-04 June 2016) event. Figures 6a-d show the LPW periapsis observation of electron density and temperature during inbound and outbound phases of the MAVEN orbits. Figures 6a-b (top panel) show the inbound phase while Figures 6c-d (bottom panel) depict the outbound phase. The mean quiet time profile is shown with a black solid line and calculated by taking the mean of quiet orbit profiles with a standard deviation during 25-28 May 2016. The event time orbits (which start on 29 May 2016 and remain up to 01 June 2016) are shown with different colors. Here, we have also selected only those disturbed orbits which are beyond the standard deviation. The inbound (Figures 6a-b) density profiles show that during the CIR event, the electron density with orbits 3238, 3240 (29 May 2016), and 3256 (01 June 2016) was significantly reduced at higher altitudes (above 350 km) associated with an enhancement in the temperature up to ~ 10000 K. The decrease in the density can also be observed for other orbit profiles between 250 to 350 km altitudes accompanied with the temperature enhancement. In addition, we have observed a sharp density gradient for the orbit 3238, where the ionopause formed at around 450 km altitude. Similarly, the outbound (Figures 6c-d) profiles with orbits 3237, 3241, and 3247 (29 May-01 June 2016) show deviation in the electron density beyond the standard deviation of the mean quiet time profile. Orbit 3247 shows a sharp density gradient from ~ 300 km, and the density was almost depleted above 350 km altitude. An enhancement of electron temperature can also be observed, which attained values above 10000 K for the mentioned orbit. The depletion in the electron density with the enhancement in the temperature indicates the formation of ionopause.

Figures 7a-n show the NGIMS observations for various ions (O^+ , O_2^+ , CO_2^+ , NO^+ , C^+ , N^+ , & OH^+) density in both inbound and outbound phases for the same orbit profiles as selected for LPW. Figures 7a-g (top panel) show the inbound phase, while Figures 7h-n (bottom panel) depict the outbound phase. The inbound O^+ density profile (Figure 7a) corresponding to the orbits 3238, 3240, and 3256 show the deviation from the mean quiet time profile with depletion from 100 cm^{-3} to 0.01 cm^{-3} above 350 km altitude. A similar trend (Figures 7b-g) is observed for other ions (O_2^+ , CO_2^+ , NO^+ , C^+ , N^+ , & OH^+) as for O^+ . However, the ionopause-like feature

is observed only in the orbits 3238 and 3240 around 450 km. Both LPW and NGIMS analyses indicate the formation of the ionopause-like feature with a sharp density gradient in the electron and ion density.

During the outbound phase (Figures 7h-n), a clear deviation from the mean quiet time profile for each ion (O^+ , O_2^+ , CO_2^+ , NO^+ , C^+ , N^+ , & OH^+) with a sharp density gradient for the orbit 3247 indicating that the ionopause formed at around 350 km. It occurred comparatively at lower altitude (~350 km) compared to the inbound phase (~450 km). During the outbound phase, the electron and ion density depletions were found in a greater number of orbit profiles compared to the inbound phase. This indicates that the ionosphere was highly variable during the outbound phase compared to the inbound phase.

3.4 Comparison of the impact of CMEs and CIRs on the Martian ionosphere

In previous sections, we presented specific cases of the ionospheric electron and ion density profiles, which showed the deviation from mean quiet time during the passage of CME and CIR events in the Martian ionosphere. In this section, we have performed a comparative analysis of the effect of several CME and CIR events on the Martian ionosphere. For this, we have extensively analyzed 15 events each. The list of CMEs and CIRs is provided in Table 1. By critically analyzing those 15 CME and 15 CIR events, we have selected 60 highly disturbed orbits during inbound as well as 60 highly disturbed orbits during outbound phases.

In order to address the differences (if any) between CME and CIR events in terms of their ionospheric impact and species variation in the Martian ionosphere, we have explored the variations of electron density, temperature, and ion density. We have calculated the mean of the ion and electron density with mean absolute deviation (MAD) for all major disturbed orbits separately for all CMEs and CIRs. Figures 8a-d show the collective average profiles for electron density and temperature using LPW periapsis measurements. Figures 8a-b (top panel) represent the inbound phase and Figures 8c-d (bottom panel) represent the outbound phase. The red color profile represents the mean electron density and temperature for 60 major disturbed orbits during 15 CMEs, while the red shaded area indicates the MAD. The same analysis has been carried out for 60 major disturbed orbits during 15 CIRs, which is represented by the blue color profiles with blue shaded area in the same figure. During the inbound phase, the difference between the mean electron density during CIRs and CMEs is less, and a similar trend can also be observed for the temperature profiles (Figures 8a-b). On the other hand, during the outbound phase, we have observed a significant difference in the mean electron density during CMEs and CIRs (Figure 8c). The mean electron density (outbound phase)

during CIRs reached less than 100 cm^{-3} above 350 km, whereas it remained more than 100 cm^{-3} during CMEs. The mean electron density profiles in the outbound phase show a larger variation in comparison to the inbound phase. However, the difference in the mean temperature profiles is not significant and lies within the standard deviation of each other during both phases. From the average profile of LPW observations, the electron density during CIRs is found to be more depleted as compared to CMEs. Further, the depletion is more pronounced in the case of outbound than inbound phase.

Using NGIMS observations, we have selected seven ions (four lighter ions: O^+ , C^+ , N^+ , & OH^+ and three heavier ions: O_2^+ , CO_2^+ , & NO^+) in order to investigate their variations during CMEs and CIRs. We have performed identical analyses by considering the same 60 major disturbed orbits. Figure 9 shows the variation of the mean ion density as a function of altitude. Figures 9a-g (top panel) show the inbound and Figures 9h-n (bottom panel) represent the outbound phase observations. For the inbound phase (Figure 9a), a significant difference in the O^+ mean density profile can be observed above 240 km. The mean density was lesser during CIRs (blue) compared to the CMEs (red). There was more than one order of magnitude difference in the mean density above 450 km. The similar trend (Figures 9b-d & Figures 9e-g) can also be observed for both heavier ions (O_2^+ , CO_2^+ , & NO^+) and lighter ions (C^+ , N^+ , & OH^+). The blue profile (CIRs) shows the lesser magnitude of mean ion density in comparison to the red profile (CMEs). The difference between two profiles is not significant below 250 km however, it became larger above this altitude.

During the outbound phase (Figure 9h), the blue and red profiles for O^+ ion nearly coincide up to 200 km altitude. Above 200 km, the mean ion density profiles show a large difference in magnitude. The other lighter ions (C^+ , N^+ , & OH^+) followed a similar trend (Figures 9i-n). For heavier ions (O_2^+ , CO_2^+ , & NO^+) the difference between the blue and red profiles is much more significant at all altitudes (Figures 9i-k). The blue profile (CIRs) shows a lesser magnitude of the mean ion density in comparison to the red profile (CMEs). In addition, the difference between blue and red profiles are more significant during the outbound phase as compared to the inbound phase. These observations also show that the mean peak altitude of lighter ions during the CIR events was lower in comparison to the CME events in both inbound and outbound phases. The difference in the mean peak altitudes during CMEs and CIRs (inbound phase) for lighter ions (O^+ , C^+ , N^+ , & OH^+) range from 20 to 60 km can be observed. Similarly, the difference occurs during the outbound phase, ranging from 10 to 45 km for the lighter ions. The mean peak density also shows the difference for lighter ions in both inbound

and outbound phases. Table 2 provides the details about the mean peak altitude with peak density for all the lighter ions.

In this study, we have observed that the ionospheric density got more depleted during CIRs in comparison to CMEs. In addition, the depletion in the mean density is more significant during the outbound in comparison to the inbound phase for both CMEs and CIRs. The above results provide us an insight that the impact of CIRs is more pronounced as compared to CMEs.

4. Discussion

The earlier studies suggest that the Martian ionosphere is greatly impacted by both CME and CIR events (Ergun et al. 2006; Jakosky 2015; Richardson 2018; Dubinin et al. 2019; Krishnaprasad et al. 2019; Thampi et al. 2021). In our study, we presented a comparative study of the differential impact of the CMEs and CIRs on the Martian ionosphere. The depletion in the electron and ion density is more pronounced during the outbound in comparison to the inbound phase for the CME (Figures 4 & 5). The depletion began at a lower altitude of nearly 230 km on the night side (outbound), which became more significant at higher altitudes. The electron density decreased lower than 100 cm^{-3} associated with the enhancement in the electron temperature. However, the electron density below 100 cm^{-3} can increase the errors in the LP temperature measurements (Andersson et al. 2015). Therefore, we cannot infer any exact correspondence between density and temperature for such a low electron density. We also observed a sharp decrease in the electron density in the orbits 7826 (outbound) and 7825 (inbound) during the CME event (03-05 October 2018). This sudden decrease in the electron density associated with the temperature enhancement was an ionopause-like feature as reported earlier (Cano et al. 2020). Apart from the electron depletion, Krishnaprasad et al. (2019) and Thampi et al. (2018, 2021) reported the depletion in the ion densities (O^+ and O_2^+) during individual CME and CIR events. In the present study, the depletion of ions (O^+ , O_2^+ , CO_2^+ , NO^+ , C^+ , N^+ , & OH^+) has been observed during the events. In addition, we have observed that the ionopause formed at a higher altitude ($\sim 450 \text{ km}$) in the inbound phase compared to the outbound phase ($\sim 400 \text{ km}$). The CME event during 03-05 October 2018 was a slow CME with a solar wind velocity of $\sim 500 \text{ km/s}$ and peak dynamic pressure of $\sim 3 \text{ nPa}$. Lower dynamic pressure led to lesser compression on the dayside (inbound), which led to the formation of ionopause at higher altitudes. The ionopause in this event was at a lower altitude for outbound (nightside). The lower ionopause altitude might be due to the electron impact ionization and the variable ionosphere in the nightside (Girazian et al. 2017). Similarly, during the CIR event (29 May-04 June 2016), we have observed ionopause for both inbound and outbound phases.

Ionopause formed at a lower height (~350 km) during the outbound phase in comparison to the inbound phase (~450 km). Both specific CME and CIR events had comparable peak dynamic pressure. However, we have observed electron and ion density depletions in a greater number of orbits in case of CIR. Generally, CIR event continued for a longer time compared to the CME event (as observed from in Figures 2 & 3). Therefore, the solar wind interacted with the constituents of the Martian ionosphere for a longer duration during the CIR event, resulting in more electron and ion density depletions. This is clearly evident from Figures 6 & 7.

In this paper, we have also presented a comparative analysis of the Martian ionospheric response to incoming CMEs and CIRs during the declining phase (2015-2019) of Solar cycle 24. We have extensively analyzed ionospheric variation in both inbound and outbound phases during 15 CMEs and 15 CIRs. During inbound phase, MAVEN monitored the dayside to dusk sectors in most of the CMEs and CIRs. Whereas during outbound phase, MAVEN monitored dusk to nightside sectors in most of the CMEs and CIRs. Due to this, there is a significant difference in ion density profiles during inbound and outbound phases (Figures 8 & 9). In addition, our analyses (for 15 CME and 15 CIR events) clearly indicate that the Martian ionospheric depletion is more significant during CIRs in comparison to the CMEs (Figures 8 & 9). The difference between mean density profiles (shown in red and blue colors) during CMEs and CIRs is less pronounced in the inbound phase as compared to the outbound phase. The lesser difference in mean density profiles during the inbound phase might be due to consistent ion production by photoionization and ion neutral chemistry during daytime. During the inbound and outbound phases, the mean peak altitude for all lighter ions (O^+ , C^+ , N^+ , & OH^+) existed at a lower altitude during CIRs as compared to CMEs. During CIRs, O^+ inbound mean peak altitude and density (225 km and 319.58 cm^{-3}) were less in comparison to the CMEs (255 km and 619.13 cm^{-3}). It has been reported that during the moderate solar cycle, the peak density of O^+ lies nearly at 300 km (Withers et al. 2015). Interestingly, it occurred at a lower altitude in the present case. During both CMEs and CIRs, the mean peak altitude of lighter ions for the outbound was always lower compared to the inbound phase. The peak density of the heavier ions (O_2^+ , CO_2^+ , & NO^+) mostly was at around 110-130 km as reported by Bouger et al. (2015). Since MAVEN measured the ionospheric plasma mostly between 150-500 km altitude range, we are unable to comment on the mean peak altitude with peak density of the heavier ions. The mean solar wind dynamic pressure was 1.03 nPa during the 15 CIRs, which is greater than that during the 15 CMEs (0.79 nPa). Thus, it led to more compression of the ionosphere, resulting in a lower peak altitude for lighter ions during the CIRs, as compared to the CMEs. In addition to the solar dynamic pressure, IMF can also play an important role in

the variation of the Martian ionosphere. In the previous studies, it is observed that during CIRs, the magnetic field alters its orientation, due to which oppositely directed magnetic field lines can cross each other while draped around the planet Mars (Edberg et al. 2010; Cravens et al. 2020). This leads to a reconnection escape mechanism which accelerates the plasma and hence could be one of the factors to enhance the escape rate. Therefore, both the dynamic pressure and reconnection at higher altitudes play an important role to accelerate and energize the plasma from the Martian ionosphere (Ergun et al. 2006; Opgenoorth et al. 2013; Fowler et al. 2019; Girazian et al. 2019; Cano et al. 2020). There are other important factors like low-frequency plasma waves, non-thermal processes, and solar wind convection electric field which may play an important role to drive the loss processes during both events (Ergun et al. 2006; Lundin et al. 2008b). This possibility could be investigated in the future for a better understanding of the loss processes in the Martian ionosphere. Based on present analyses, we observed that the impact of the CIRs on the Martian ionospheric species is more in comparison to the CMEs. Further work is needed in order to quantify the whole ionospheric species loss during CIRs and CMEs compared to quiet time values.

5. Summary and conclusions

The impact of CMEs and CIRs on the Martian ionosphere during the declining phase (2015-2019) of Solar cycle 24 is investigated using the observations from the MAVEN datasets. The CME and CIR events were observed at Mars with the enhancements in the solar wind density, velocity, solar wind dynamic pressure, and fluctuating IMF. From our observations, we found that the specific CME (03-05 October 2018) and CIR (29 May-04 June 2016) caused significant depletion during the outbound phase as compared to the inbound phase. The sharp density gradient in plasma indicates the formation of ionopause for orbits 7825 (inbound, CME), 7826 (outbound, CME), 3238 (inbound, CIR), and 3247 (outbound, CIR). Despite the comparable peak dynamic pressure, the depletion in the plasma density occurs for a greater number of orbit profiles during specific CIR compared to CME. In addition, this paper provides a comparative average scenario of the Martian ionospheric response during 15 CMEs and 15 CIRs. The average analyses for ionospheric species suggest that during CIRs, the ionosphere is found to be more depleted compared to CMEs. The peak mean altitude and density for lighter ions have lower values during CIRs in comparison to CMEs. Further, the depletion is more pronounced in case of the outbound phase with lower mean altitude and density compared to the inbound phase. The higher mean dynamic pressure during CIRs compared to CMEs would be one of

the plausible reasons for more depletion of the upper ionosphere in Mars during CIRs. Thus, the analyses indicate more impact of CIRs on the Martian ionosphere in comparison to CMEs.

Acknowledgements

We sincerely acknowledge the MAVEN team for the data. We also acknowledge the WSA-ENLIL+CONE Model for simulation snapshots. L. Ram acknowledges the fellowship from the Ministry of Education, Government of India for carrying out this research work. D. Rout acknowledges the support from Humboldt Research Fellowship for Postdoctoral Researchers (Humboldt foundation grants PSP D-023-20- 001). R. Rathi acknowledges the fellowship from the Innovation in Science Pursuit for Inspired Research (INSPIRE) programme, Department of Science and Technology, Government of India. S. Mondal acknowledges fellowship from Physical Research Laboratory. This work is also supported by the Ministry of Education, Government of India.

Data Availability

We have used the DONKI database (<https://ccmc.gsfc.nasa.gov/donki/>) for space weather forecast information. The MAVEN datasets used in our work are taken from the NASA Planetary Data System (<https://pds.nasa.gov/>) and downloaded using the Python Data Analysis and Visualization tool (PyDIVIDE; <https://github.com/MAVENSDC/Pydivide>). The WSA-ENLIL+Cone model simulation snapshots are used from ENLIL Solar Wind Prediction (<https://helioweb.net/>).

References:

Andersson L. et al., 2015, *Space Sci. Rev.*, 195, 173

Belcher J. W., Davis Jr. L., 1971, *J. Geophys. Res.*, 76(16), pp.3534-3563

Benna M., P. R. Mahaffy, J. M. Grebowsky, J. L. Fox, R. V. Yelle, B. M. Jakosky, 2015, *Geophys. Res. Lett.*, 42, 8958–8965

Borovsky J. E., Denton M. H., 2006, *J. Geophys. Res.: Space Physics*, 111(A7)

Bougher et al., 2015, *J. Geophys. Res.: Planets*, 120(2), pp.311-342

Burlaga L. F., 1974, *J. Geophys. Res.*, 79(25), pp.3717-3725

Cane H. V., Richardson I. G., 2003, *J. Geophys. Res.: Space Physics*, 108(A4)

Cano et al., 2020, *J. Geophys. Res.: Space Physics*, 125(9), p. e2020JA028145

Chen P.F., 2011, *Living Rev. Sol. Phys.* 8, 1

Chu F. et al., 2021, *J. Geophys. Res.: Planets*, 126, e2021JE006936

Cloutier P. A., McElroy M. B., Michel F. C., 1969, *J. Geophys. Res.*, 74(26), pp.6215-6228

Connerney J. E. P. et al., 2015, *Geophys. Res. Lett.*, 42(21), pp.8819-8827

Connerney J. E. P., Espley J., Lawton P. et al., 2015, *Space Sci. Rev.* 195, 257–291

Cravens T. E. et al., 2020, *J. Geophys. Res.: Space Physics*, 125(9), p.e 2020JA028036

Dubinin E., Fraenz M., Woch J., Duru F., Gurnett D., Modolo R., Barabash S., Lundin R., 2009, *Geophys. Res. Lett.*, 36(1)

Dubinin E., Sauer K., Baumgartel K., Lundin R., 1997, *Adv. Space Res.*, 20(2), pp.149-153

Edberg et al., 2010, *Geophys. Res. Lett.*, 37(3)

Ergun R. E. et al., 2006, *Geophys. Res. Lett.*, 33(14)

Fowler C. M. et al., 2019, *J. Geophys. Res.: Space Physics*, 124(4), pp.3021-3035

Fox J., Dalgarno A., 1979, *J. Geophys. Res.*, 84(A12), p.7315

Geyer P., Temmer M., Guo J., Heinemann S., 2021, *A&A*, 649, p.A80

Girazian Z. et al., 2019, *Geophys. Res. Lett.*, 46(15), pp.8652-8662

Gopalswamy N., 2006, *J. Astrophys. Astron.*, 27(2), pp.243-254

Gosling J., 1990, *Physics of magnetic flux ropes*, 58, pp.343-364

Gosling J., Forsyth R., 2001, *Space Sci. Rev.*, 97(1/4), pp.87-98

Gosling J., McComas D., Phillips J., Bame S., 1991, *J. Geophys. Res.*, 96(A5), p.7831

Gosling J., Pizzo V., 1999, *Space Science Reviews* 89, 21–52

Halekas J. S., Taylor E. R., Dalton G., Johnson G., Curtis D. W., McFadden J. P., et al., 2015, *Space Science Reviews*, 195(1–4), 125–151

Halekas J. S. et al., 2017, *J. Geophys. Res.: Space Physics*, 122(1), pp.547-578

Hara et al., 2011, *J. Geophys. Res.: Space Physics*, 116(A2)

Huang et al., 2019, *ApJ*, 879 118

Jakosky B. M. et al., 2015, *Science*, 350(6261), p. aad0210F

Jian L., Russell C. T., Luhmann J. G., Skoug R. M., 2006, *Solar Physics*, 239(1), pp.393-436

Krishnaprasad C., Thampi S. V., Bhardwaj A., 2019, *J. Geophys. Res.: Space Physics*, 124, 6998–7012

Lee et al., 2017, *J. Geophys. Res.: Space Physics*, 122(3), pp.2768-2794

Lundin R. et al., 1990, *Geophys. Res. Lett.* 17(6):873–876

Lundin R. et al., 2008b, *Geophys. Res. Lett.* 35

Ma Y. J., Nagy A. F., 2007, *Geophys. Res. Lett.*, 34(8)

Mahaffy P. R. et al., 2015, *Space Sci. Rev.*, 195(1), pp.49-73

Mays M. L. et al., 2015, *ApJ*, 812(2), p.145

McElroy M. B., Kong T. Y., Yung Y. L., 1977, *J. Geophys. Res.*, 82(28), pp.4379-4388

Michel F. C., 1971, *Rev. Geophys.*, 9(2), pp.427-435

Neugebauer M., Goldstein R., Goldstein B. E., 1997, *J. Geophys. Res.: Space Physics*, 102(A9), pp.19743-19751

Odstrcil D., 2003, *Adv. Space Res.*, 32(4), pp.497-506

Opgenoorth H. J. et al., 2013, *J. Geophys. Res.: Space Physics*, 118(10), pp.6558-6587

Rout et al., 2017, *Geophys. Res. Lett.*, 44

Richardson I. G., 2018, *Living Rev. Sol. Phys.*, 15(1), pp.1-95

Russell C. T., Shinde A. A., Jian L., 2005, *Adv. Space Res.*, 35(12), pp.2178-2184

Schunk R., Nagy A., 2009, Cambridge university press

Smith E. J., Wolfe J. H., 1976, *Geophys. Res. Lett.*, 3(3), pp.137-140

Thampi S. V., Krishnaprasad C., Bhardwaj A., Lee Y., Choudhary R. K., Pant T. K., 2018, *J. Geophys. Res.: Space Physics*, 123(8), pp.6917-6929

Thampi S. V., Krishnaprasad C., Nampoothiri G. G., Pant T. K., 2021, *MNRAS*, 503(1), pp.625-632

Tousey R., 1973, In *Space Research Conference* (Vol. 2, pp. 713-730)

Vogt M. F. et al., 2015, *Geophys. Res. Lett.*, 42(21), pp.8885-8893

Wei Y. et al., 2012, *J. Geophys. Res.: Space Physics*, 117(A3)

Wimmer-Schweingruber R. F. et al., 2006, Springer, New York, NY (pp. 177-216)

Withers P., Vogt M. F., Mahaffy P., Benna M., Elrod M., Jakosky B., 2015, *Geophys. Res. Lett.*, 42(21), pp.9071-9079

Withers P. et al., 2018, J. Geophys. Res.: Space Physics, 123, 4171–4180

Zhao D. et al., 2021, ApJ, 923(1), p.4

Zurbuchen T. H., Richardson I. G., 2006, Springer, New York, NY, pp. 31-43

Figures:

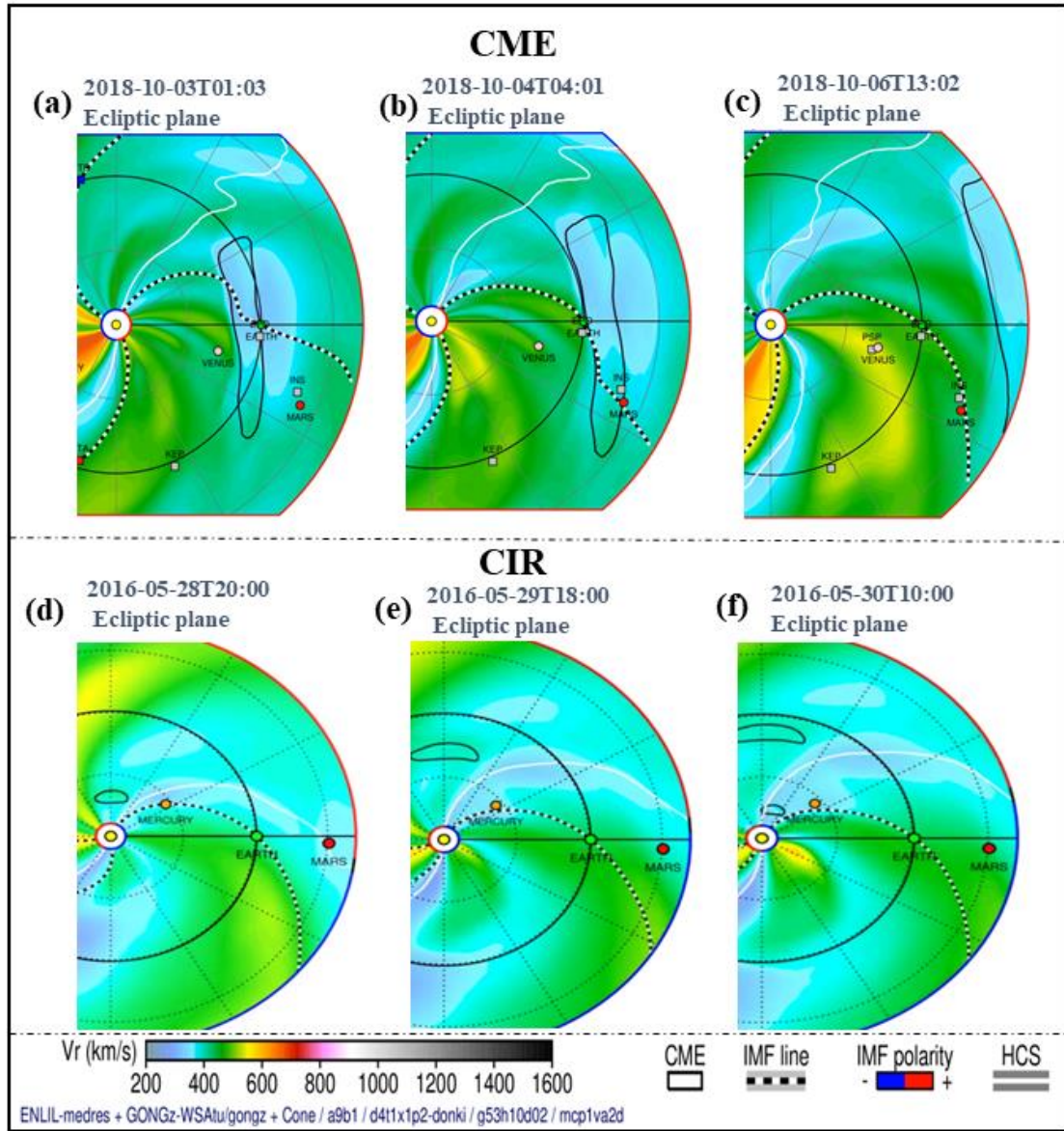


Figure 1: The WSA-ENLIL+ Cone model inner heliospheric simulation screenshots, (a) before the event (b) during the event, and (c) after the event, showing the solar wind radial velocity (color contour) and interplanetary magnetic field (IMF) during the 03-05 October 2018 CME event, and (d) before the event, (e) during the event, (f) after the event, showing the solar wind radial velocity (color contour) and interplanetary magnetic field (IMF) during the 29 May-04 June 2016 CIR event.

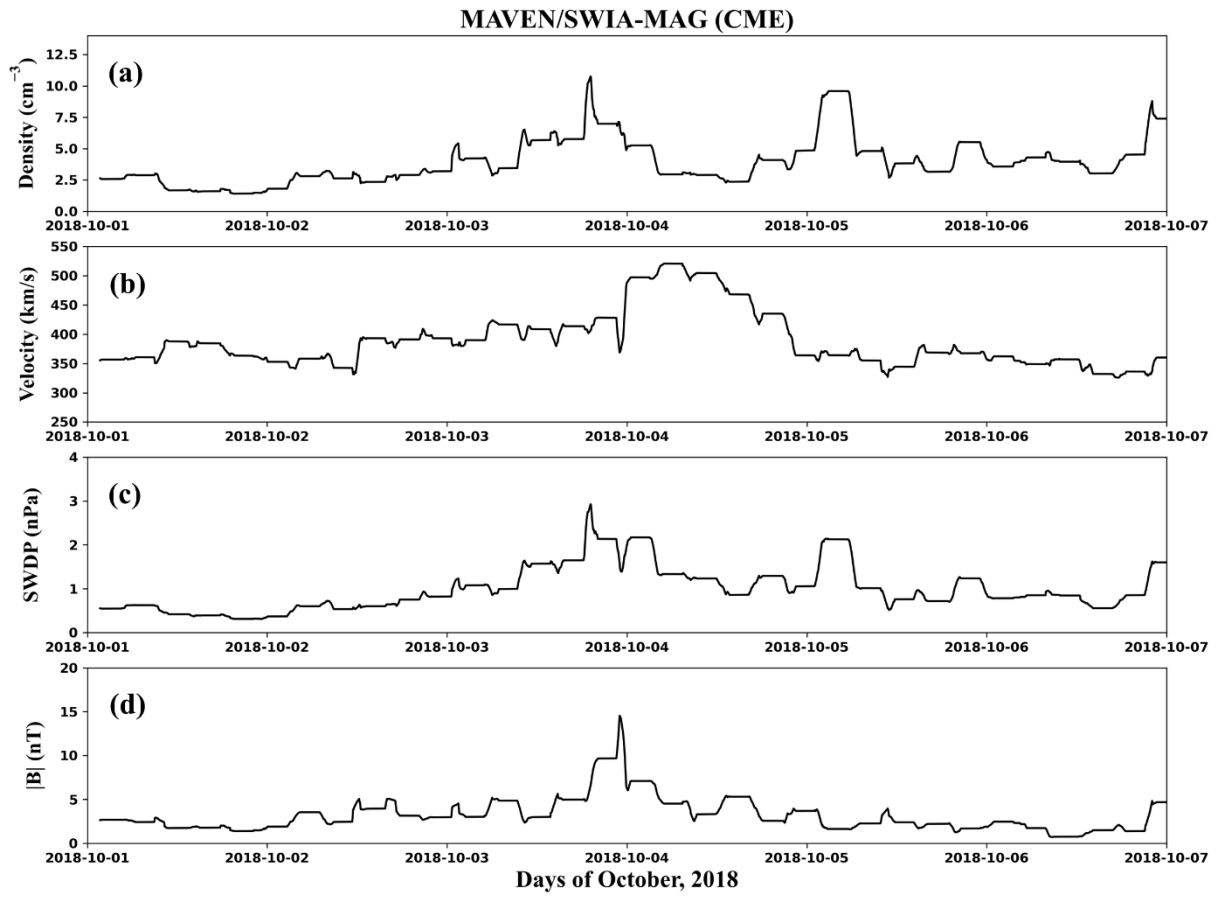


Figure 2: (a) Solar wind density, (b) solar wind velocity, (c) dynamic pressure, and (d) IMF($|\mathbf{B}|$), observations near Mars, during the 03-05 October 2018 CME event.

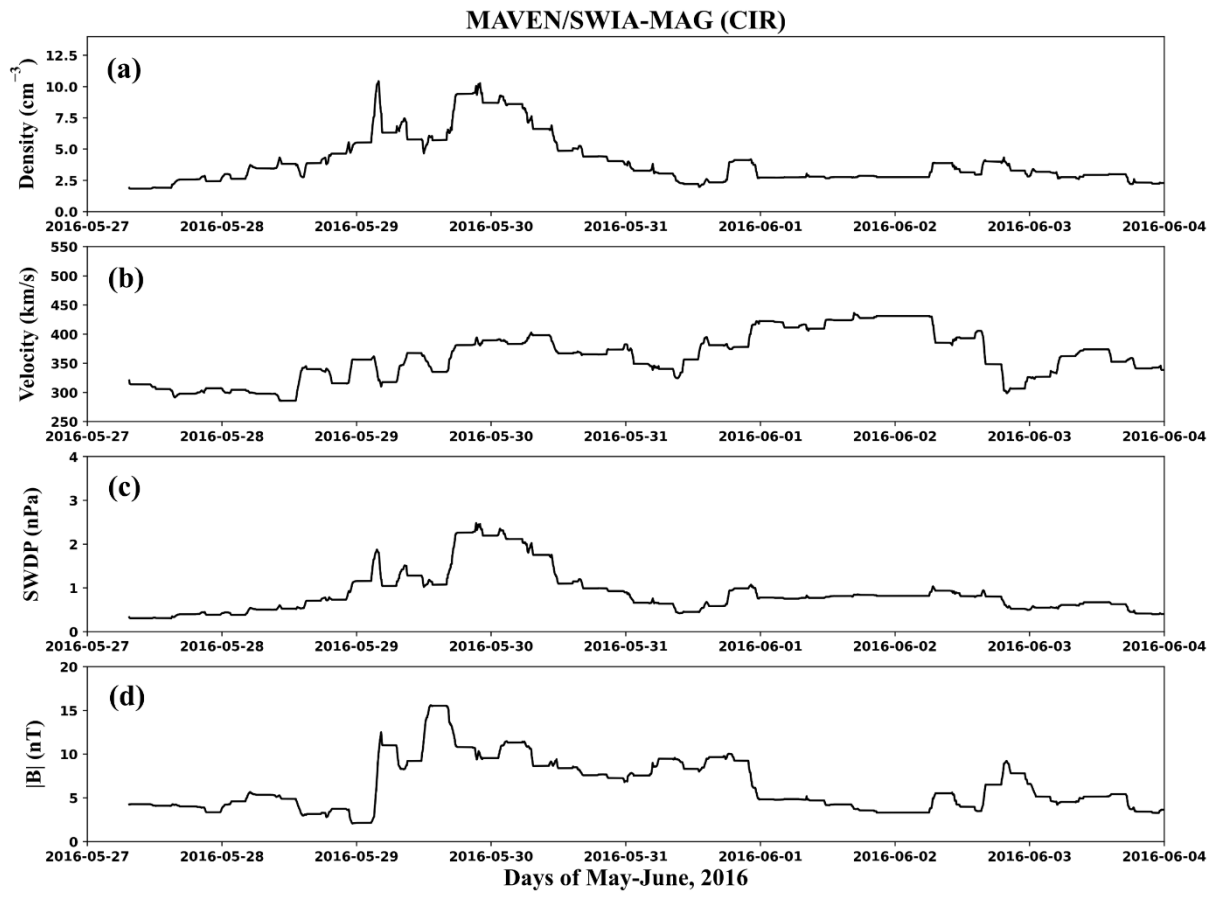


Figure 3: (a) Solar wind density, (b) solar wind velocity, (c) dynamic pressure, and (d) IMF($|\mathbf{B}|$), observations near Mars, during the 29 May-04 June 2016 CIR event.

MAVEN/LPW (CME)

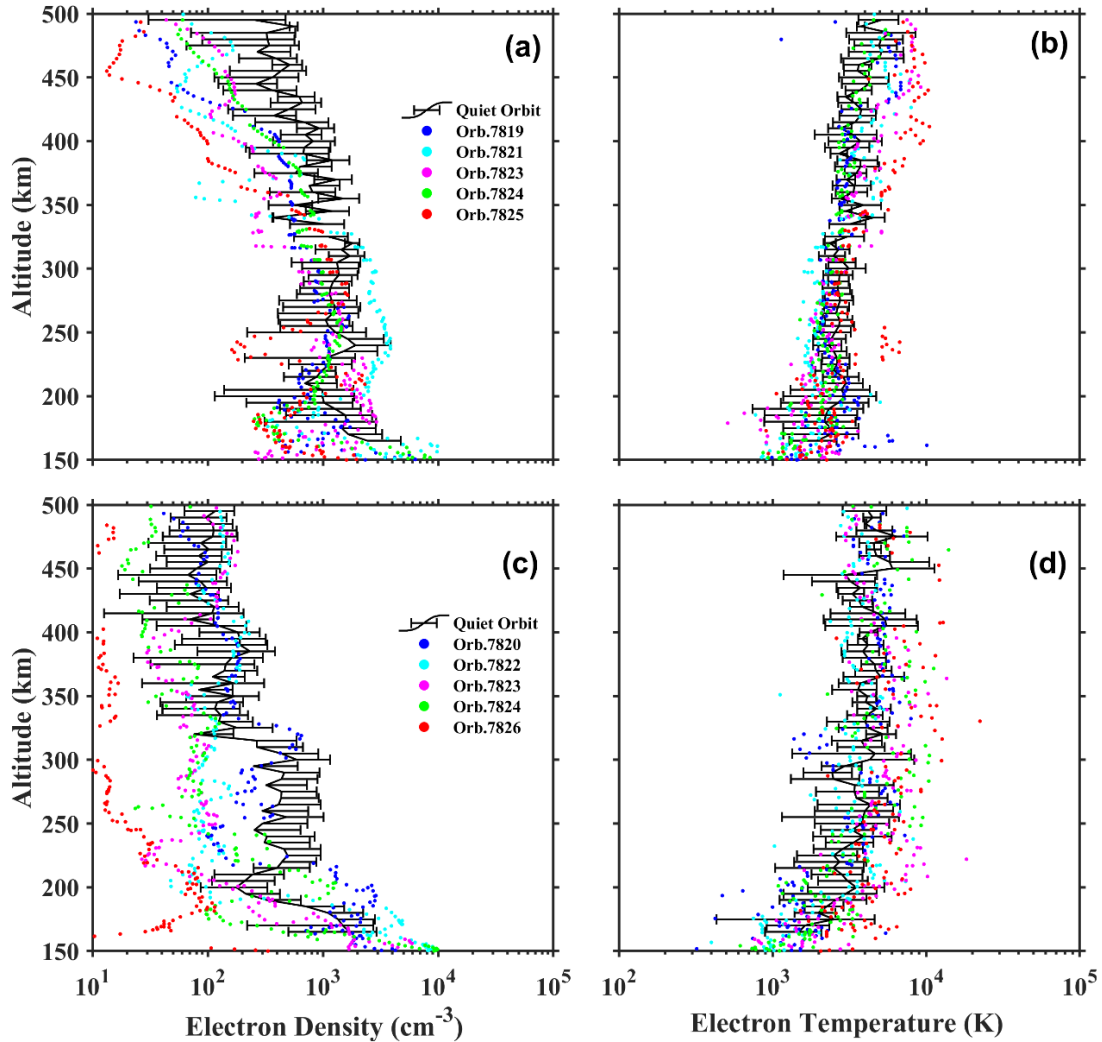


Figure 4: The Langmuir Probe and Waves (LPW), (a-b) inbound and (c-d) outbound, electron density and temperature variations as a function of altitude (150-500 km) during the 03-05 October 2018, along with the specific quiet time variation. The disturbed orbits are shown as different color dots. The mean of the quiet time profiles (orbit numbers 7806, 7807, 7810, 7815, 7817 for inbound and 7807, 7808, 7811, 7816, 7819 for outbound phase, respectively) are shown (black curve) along with the standard deviation.

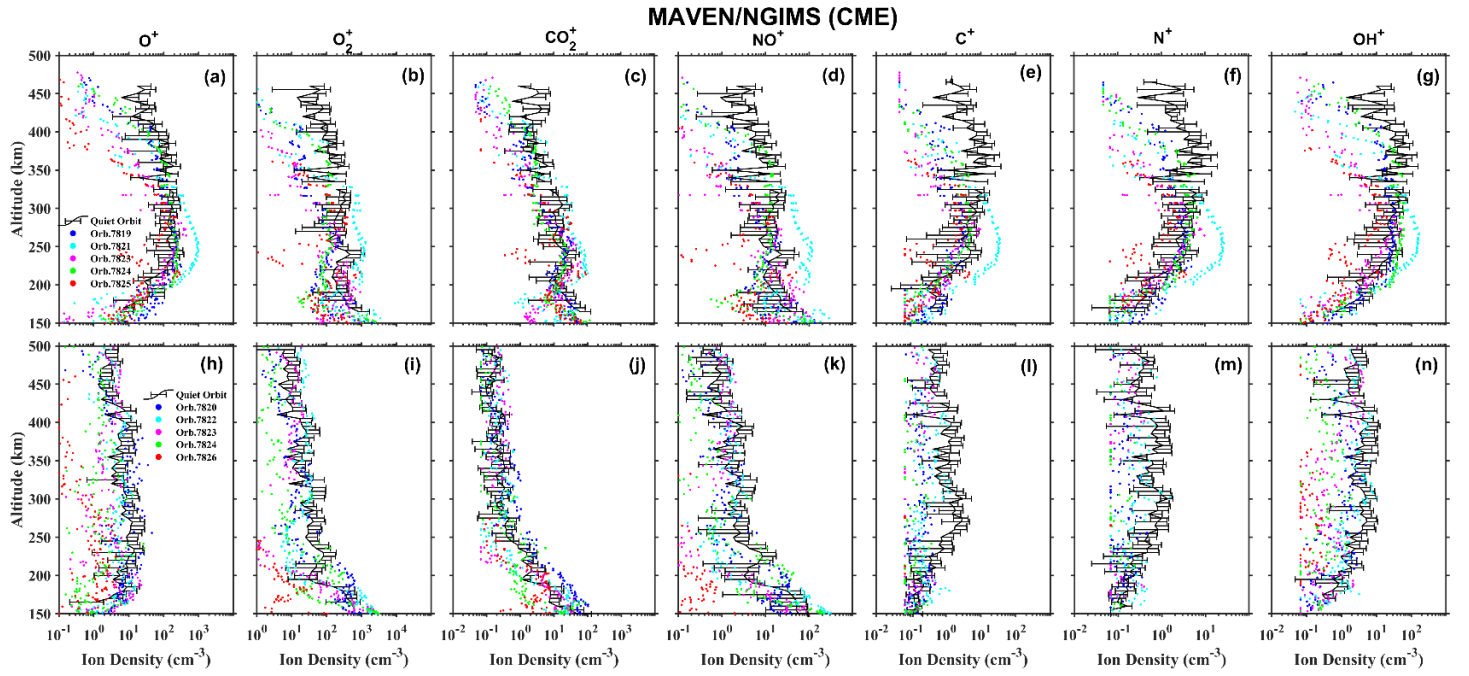


Figure 5: The Neutral Gas and Ion Mass Spectrometer (NGIMS), (a-g) inbound and (h-n) outbound, ions density variation as a function of altitude (150-500 km) during the 03-05 October 2018, along with the specific quiet time variation. The disturbed orbits are shown as different color dots. The mean of the quiet time profiles (orbit numbers 7806, 7807, 7810, 7815, 7817 for inbound and 7807, 7808, 7811, 7816, 7819 for outbound phase, respectively) are shown (black curve) along with the standard deviation.

MAVEN/LPW (CIR)

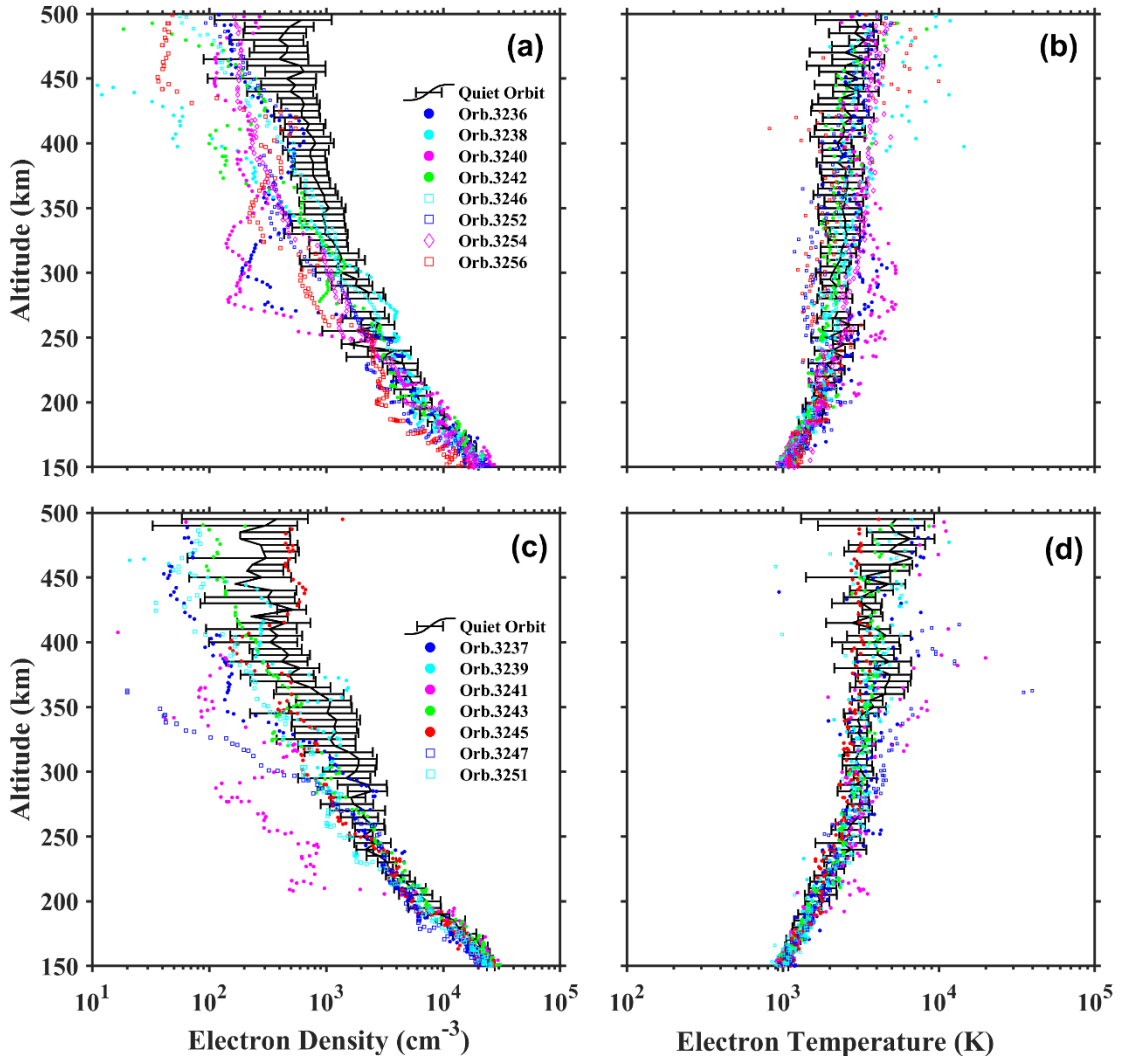


Figure 6: The Langmuir Probe and Waves (LPW), (a-b) inbound and (c-d) outbound, electron density and temperature variations as a function of altitude (150-500 km) during 29 May-04 June 2016, along with the specific quiet time variation. The disturbed orbits are shown as different color dots. The mean of the quiet time profiles (orbit numbers 3225, 3226, 3228, 3231, 3232, 3233 for inbound and 3225, 3226, 3229, 3231, 3232, 3233 for outbound phase, respectively) are shown (black curve) along with standard deviation.

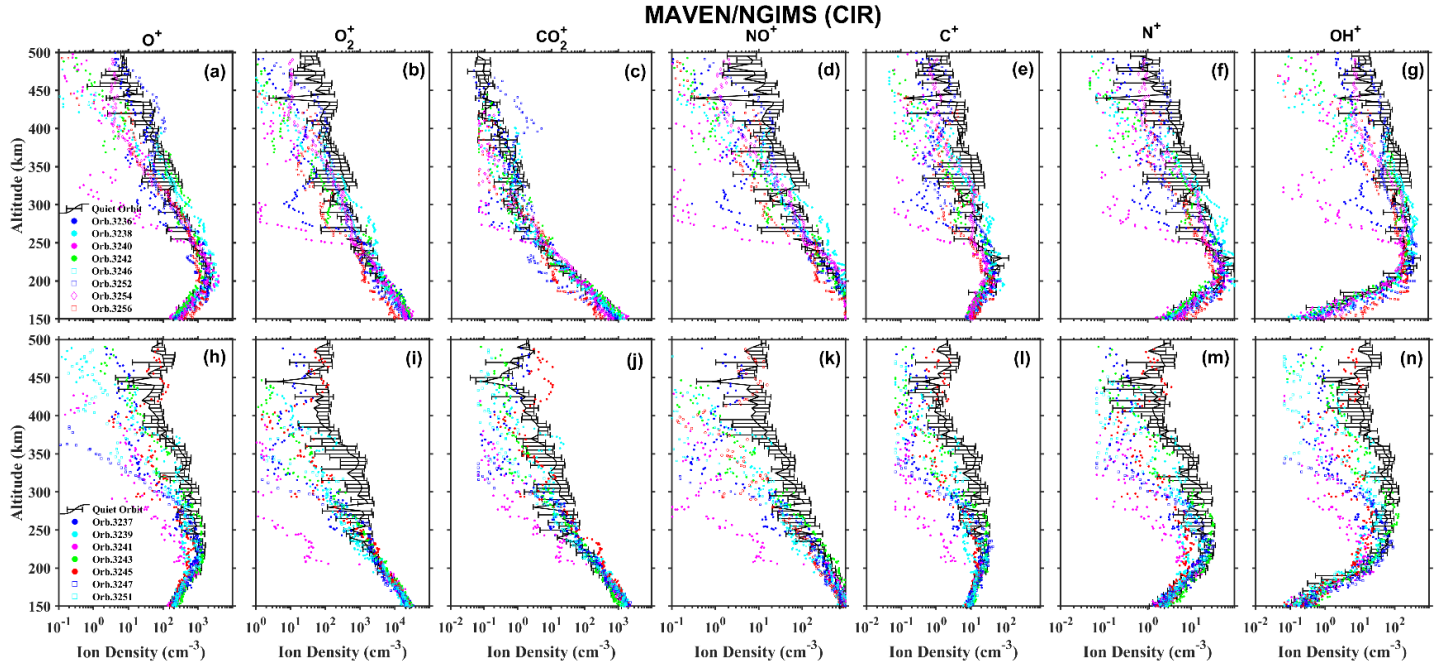


Figure 7: The Neutral Gas and Ion Mass Spectrometer (NGIMS), (a-g) inbound and (h-n) outbound, ions density variation as a function of altitude (150-500 km) during 29 May-04 June 2016, along with the specific quiet time variation. The disturbed orbits are shown as different color dots. The mean of the quiet time profiles (orbit numbers 3225, 3226, 3228, 3231, 3232, 3233 for inbound and 3225, 3226, 3229, 3231, 3232, 3233 for outbound phase, respectively) are shown (black curve) along with standard deviation.

MAVEN/LPW

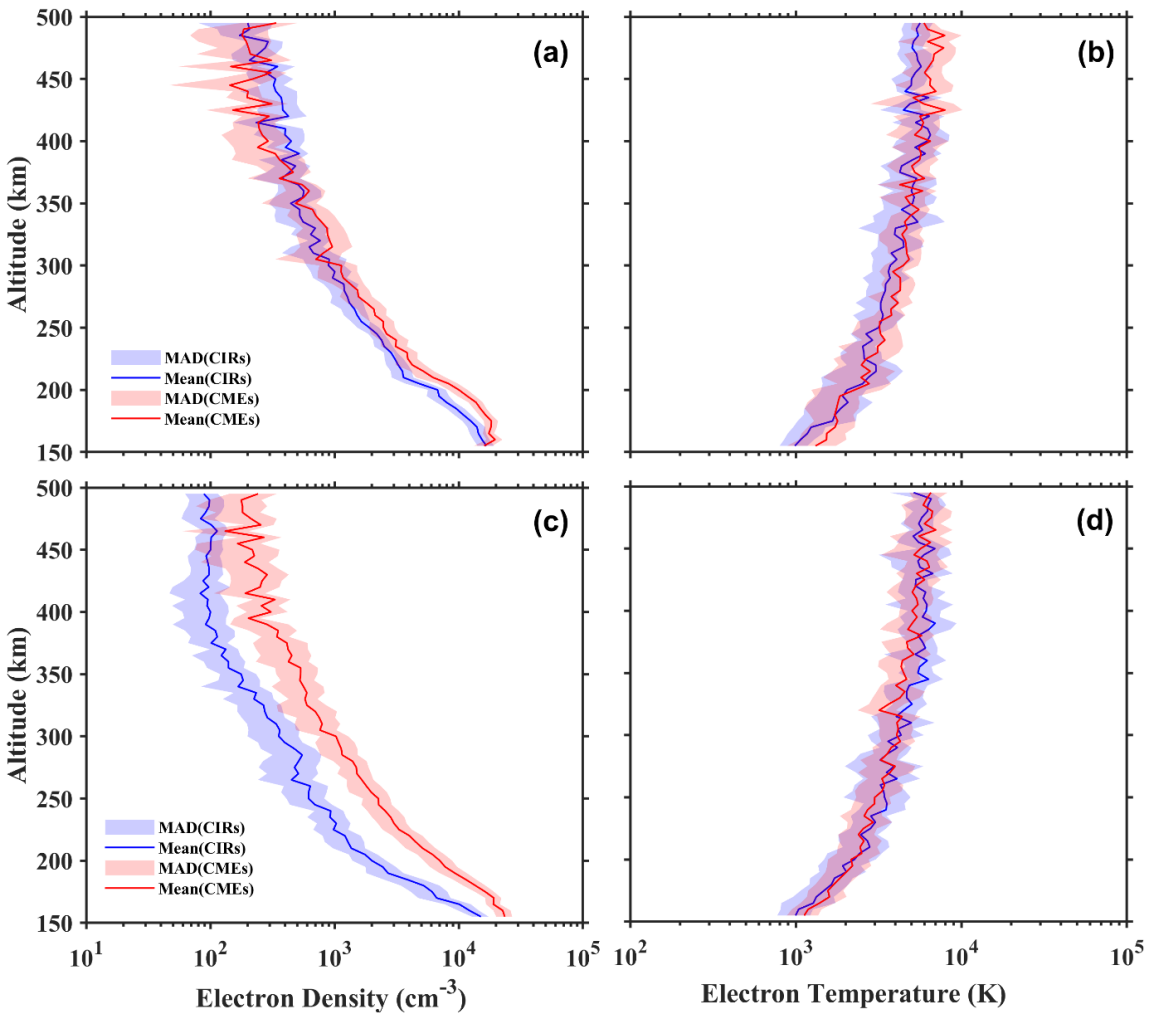


Figure 8: The Langmuir Probe and Waves (LPW), (a-b) inbound, (c-d) outbound, electron density and temperature variations as a function of altitude (150-500 km) for 60 highly disturbed orbit profiles during 15 CIRs and 15 CMEs. Red and Blue shades represent MAD (mean absolute deviations) with mean values represented as red and blue profiles.

MAVEN/NGIMS

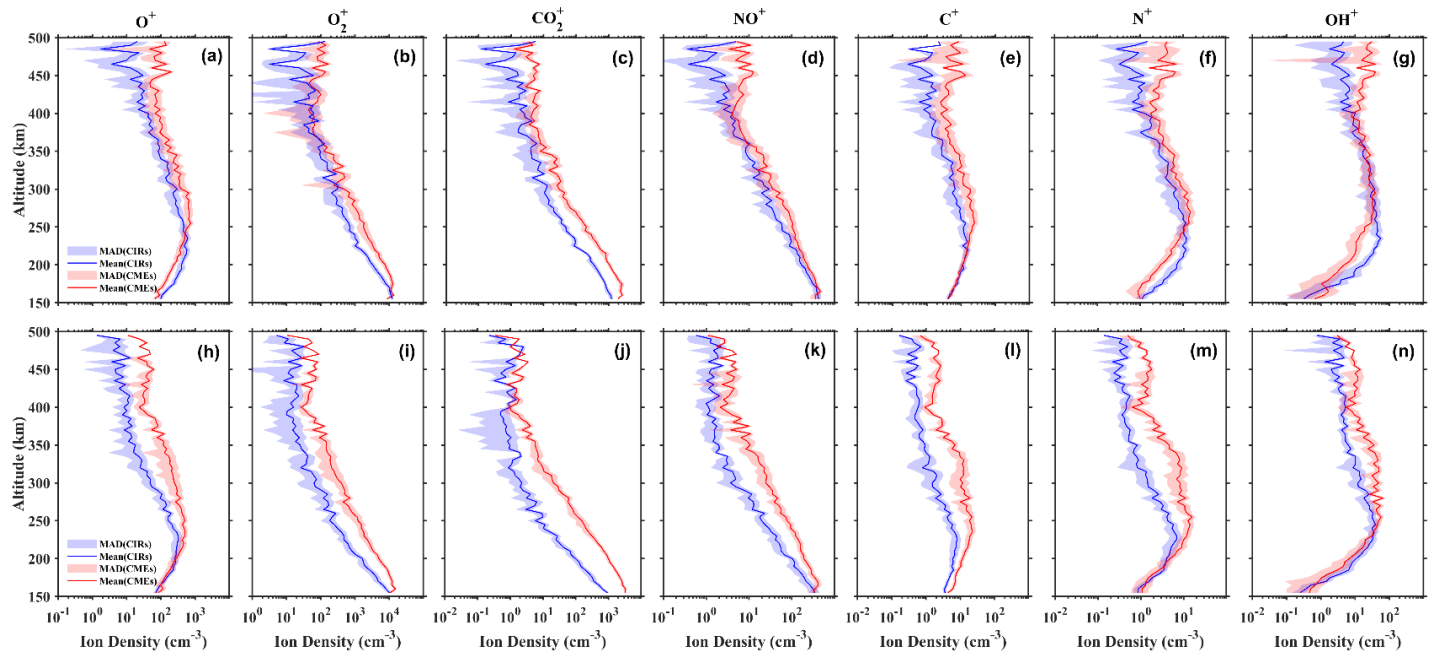


Figure 9: The Neutral Gas and Ion Mass Spectrometer (NGIMS), (a-g) inbound and (h-n) outbound, ion density variations as a function of altitude (150-500 km) for 60 highly disturbed orbit profiles during 15 CIRs and 15 CMEs. Red and Blue shades represent MAD (mean absolute deviations) with mean values represented as red and blue profiles.

Tables:

List of CMEs and CIRs (2015-2019)

	S. No.	Start Date (YYYY/MM/DD)	End Date (YYYY/MM/DD)	N_{mean} (cm⁻³)	V_{mean} (km/s)	P_{dy}_{mean} (nPa)	 B _{mean} (nT)
CME	1.	2015/03/03	2015/03/06	4.75	410.0	1.31	6.82
	2.	2015/03/08	2015/03/11	1.99	430.8	1.10	10
	3.	2015/04/22	2015/04/24	1.02	175.6	0.17	11.67
	4.	2015/05/05	2015/05/07	1.73	235.2	0.33	13.83
	5.	2015/10/04	2015/10/06	2.82	284.1	0.66	8.0
	6.	2016/09/23	2016/09/24	4.68	336.48	1.06	13.93
	7.	2016/10/05	2016/10/07	5.33	286.8	0.79	8.98
	8.	2016/11/12	2016/11/14	2.33	236.8	0.30	5.55
	9.	2017/03/03	2017/03/07	5.78	312.87	0.89	9.43
	10.	2017/07/17	2017/07/18	4.80	283.43	0.646	3.27
	11.	2018/07/18	2018/07/19	6.84	307.18	1.05	7.61
	12.	2018/09/24	2018/09/24	3.64	357.08	0.81	5.60
	13.	2018/08/27	2018/08/28	3.66	389.5	0.94	4.36
	14.	2018/10/03	2018/10/05	5.35	391.3	1.25	3.94
	15.	2019/05/07	2019/05/12	4.45	264.9	0.53	6.83
CIR	1.	2015/02/18	2015/02/20	15.92	307.98	2.53	9.42
	2.	2015/02/25	2015/02/28	10.45	293.98	1.44	6.96
	3.	2015/10/02	2015/10/03	3.12	279.22	0.61	7.76
	4.	2015/12/17	2015/12/19	5.57	441.19	1.68	8.39
	5.	2016/03/11	2016/03/15	2.21	381.84	0.66	5.65
	6.	2016/03/16	2016/03/19	1.16	303.7	0.32	3.89
	7.	2016/05/29	2016/06/04	3.01	335.3	0.61	5.18
	8.	2016/07/03	2016/07/06	2.73	410.8	0.82	3.18
	9.	2016/07/14	2016/07/18	1.51	473.9	0.59	2.0
	10.	2016/09/17	2016/09/22	2.05	461.1	0.78	4.1
	11.	2017/08/20	2017/08/21	5.38	426.93	1.49	5.44
	12.	2018/08/12	2018/08/14	4.53	361.6	0.99	2.89
	13.	2018/08/27	2018/08/31	2.47	413.1	0.72	2.96
	14.	2018/11/03	2018/11/08	5.67	391.1	1.26	6.16
	15.	2018/11/09	2018/11/14	3.46	402.6	0.91	5.92

Table 1: The values denote the mean values for solar wind density [N_{mean} (cm⁻³)], velocity [V_{mean} (km/s)], dynamic pressure [P_{mean} (nPa)], and IMF [|B|_{mean} (nT)] during 15 CMEs and 15 CIRs.

Events	I/O Phase	$[\text{O}^+]$ mean peak alt. (km) & density (cm^{-3})	$[\text{C}^+]$ mean peak alt. (km) & density (cm^{-3})	$[\text{N}^+]$ mean peak alt. (km) & density (cm^{-3})	$[\text{OH}^+]$ mean peak alt. (km) & density (cm^{-3})
CMEs	Inbound	255, 742.78	255, 24.50	265, 15.02	295, 39.10
	Outbound	235, 516.11	255, 21.83	255, 15.98	280, 66.37
CIRs	Inbound	235, 619.13	220, 14.78	230, 14.09	235, 55.95
	Outbound	225, 319.58	230, 8.06	230, 6.89	235, 40.45

Table 2: The mean peak altitude of lighter ions (O^+ , C^+ , N^+ , & OH^+) and ions density for both inbound and outbound phases during 15 CMEs and 15 CIRs events.